Interfacial Structure and Electric Field Probed by *in Situ* Electrochemical Vibrational Stark Effect Spectroscopy and Computational Modeling

Aimin Ge,[†] Pablo E. Videla,[‡] Gwendolynne L. Lee,[§] Benjamin Rudshteyn,[‡] Jia Song,[†] Clifford P. Kubiak,*,[§] Victor S. Batista,*,[‡] and Tianquan Lian*,[†]

[†]Department of Chemistry, Emory University, 1515 Dickey Dr., NE, Atlanta, Georgia 30322, United States

[‡]Department of Chemistry and Energy Sciences Institute, Yale University, 225 Prospect St., New Haven, Connecticut 06520, United States

[§]Department of Chemistry and Biochemistry, University of California, San Diego, 9500 Gilman Dr. MC 0358, La Jolla, California 92093, United States

Ⓢ *Supporting Information*

ABSTRACT: Interfacial electric fields play crucial roles in electrochemistry, catalysis, and solar energy conversion. Understanding of the interfacial electric field effects has been hindered by the lack of a direct spectroscopic method to probe of the interfacial field at the molecular level. Here, we report the characterization of the field and interfacial structure at Au/diisocyanide/aqueous electrolyte interfaces, using a combination of *in situ* electrochemical vibrational sum frequency generation (SFG) spectroscopy, density functional theory (DFT) calculations, and molecular dynamics (MD) simulations. For 1,4-phenylene diisocyanide (PDI), 4,4′-biphenyl diisocyanide (BPDI), and 4,4″-*p*-terphenyl diisocyanide

(TPDI), our results reveal that the frequency of the gold-bound NC stretch mode of the diisocyanide self-assembled monolayer (SAM) increases linearly with the applied potential, suggesting that SFG can be an *in situ* probe of the strength of the electric field at electrode/electrolyte interfaces. Using DFT-computed Stark tuning rates of model complexes, the electric field strength at the metal/SAM/electrolyte interfaces is estimated to be $10^8 - 10^9$ V/m. The linear dependence of the vibrational frequency (and field) with applied potential is consistent with an electrochemical double-layer structure that consists of a Helmholtz layer in contact with a diffused layer. The Helmholtz layer thickness is approximately the same as the molecular length for PDI, suggesting a well-ordered SAM with negligible electrolyte penetration. For BPDI and TPDI, we found that the Helmholtz layer is thinner than the monolayer of molecular adsorbates, indicating that the electrolyte percolates into the SAM, as shown by molecular dynamics simulations of the Au/PDI/electrolyte interface. The reported analysis demonstrates that a combination of *in situ* SFG probes and computational modeling provides a powerful approach to elucidate the structure of electrochemical interfaces at the detailed molecular level.
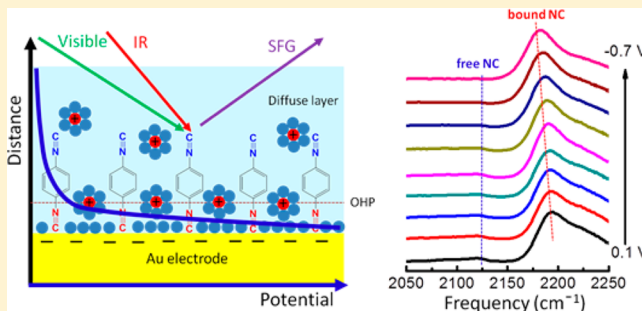
1. INTRODUCTION

Interfacial electric fields, applied externally or induced by photoexcitation, are known to play crucial roles in electrochemistry, catalysis, and solar energy conversion processes.[1−8] Because of the difficulty of a direct measurement of the interfacial electric field strength, a fundamental understanding of its effects on reaction dynamics is still lacking. In conventional electrochemical measurements, interfacial field strengths are often inferred from measured macroscopic quantities (capacitance and current−voltage curves) through models of electrochemical double-layer structure, such as the Gouy−Chapman−Stern model.[1] However, it is highly desirable to develop spectroscopic probes at the molecular level to measure directly the field strength and its spatial distribution. The vibrational Stark effect (i.e., the influence of the local

electric field on the vibrational frequency of a normal mode) has been shown to be a powerful molecular spectroscopic probe of the local field strength.[9−15] The vibrational Stark effect has been successfully investigated to explore the electric fields in proteins, providing important insights into the roles of electrostatic potentials in enzyme catalysis.[16−19] The vibrational Stark effect has also been used to study electric fields at electrochemical interfaces.[20−23] Because of the challenge in measuring the vibrational spectrum of a monolayer (or submonolayer), many previous studies have utilized surface-enhanced Raman spectroscopy (SERS), including different

vibrational probes adsorbed on rough electrodes.[20−22] However, the complexity of such interfaces has hindered a quantitative investigation of electrochemical double-layer structure and the spatial variation of the interfacial field.

Here, we characterize the interfacial structure and field strength of planar Au electrode/electrolyte interfaces using a combination of *in situ* electrochemical vibrational sum frequency generation (SFG) spectroscopy, density functional theory (DFT) calculations, and molecular dynamics (MD) simulations. We focus on three aromatic diisocyanides (Figure 1) with isocyanide groups probing the field across the
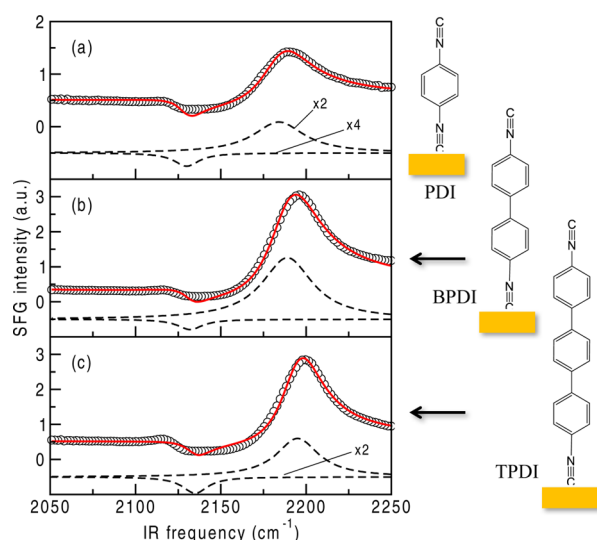

Figure 1. SFG spectra of Au/diisocyanide/air interfaces. Left: representative SFG spectra (open circles). Right: schematic structure of (a) PDI, (b) BPDI, and (c) TPDI adsorbed on the Au electrode (yellow). Solid red lines are simulated SFG spectra based on DFT calculations, whereas broken lines correspond to the resonance components used in the fit (offset for clarity).

Helmoholtz bilayer at increasing distances from the Au surface, including 1,4-phenylene diisocyanide (PDI), 4,4′-biphenyl diisocyanide (BPDI), and 4,4″-*p*-terphenyl diisocyanide (TPDI). Aromatic para-substituted diisocyanides have been shown to covalently bind on planar gold electrode surfaces through only one isocyanide (NC) group at high surface coverage, forming ordered self-assembled monolayers (SAMs).[24−32] Here, we probe the frequency shift of the NC groups under applied potentials, using *in situ* electrochemical SFG spectroscopy.[33−38] Since SFG does not require background subtraction or rough metal surfaces (or metal nanoparticles), as does electrochemical IR spectroscopy[39] or SERS,[40−42] respectively, it can be used as a sensitive probe of adsorbates on planar electrodes.[43−49] Our results show that the frequency of the surface bound NC stretch model increases linearly with applied potentials (from −0.7 to +0.1 V vs Ag/AgCl in 0.1 M NaClO$_4$ aqueous electrolyte), indicating a linear dependence with applied bias of the electric field at the surface. Using Stark tuning rates computed by density functional theory (DFT), the electric field strength at the metal/SAM/electrolyte interface can be determined. Furthermore, assuming an electrical double-layer structure that consists of a Helmholtz and diffused layer, it can be shown that the slope of the linear dependence of measured NC stretch frequency on applied bias is a direct probe of the thickness of the Helmholtz layer, which

can be used to probe the extent of electrolyte percolation into the SAM layers of PDI, BPDI, and TPDI. Finally, we carried out molecular dynamics simulations to provide further molecular level insight into the structure of the interface.

2. RESULTS AND DISCUSSION

SFG Spectra at Au/Air Interface. Figure 1 shows the SFG spectra of diisocyanide SAMs absorbed on gold films in the NC stretching region. Details of the preparation of the SAM of PDI, BPDI, and TPDI on Au films (SAM/Au) as well as the experimental setup for the SFG measurement are provided in the Supporting Information. The vibrational SFG intensity from the sample can be modeled according to[33−38]

$$I_{SFG} \propto |\chi^{(2)}_{NR,eff} + \chi^{(2)}_{R,eff}|^2$$

$$= \left| A_{NR,eff} e^{i\delta} + \sum_q \frac{A_{q,eff}}{\omega_{IR} - \omega_q + i\Gamma_q} \right|^2 \tag{1}$$

where $\chi^{(2)}_{R,eff}$ and $\chi^{(2)}_{NR,eff}$ are the effective resonant and nonresonant nonlinear susceptibility tensor elements, respectively, which are products of susceptibility tensor elements and Fresnel coefficients. $\chi^{(2)}_{R,eff}$ arises from the adsorbate and can be approximated as a sum of Lorentzian functions, where $A_{q,eff}$, ω_q, and Γ_q are the effective amplitude, frequency, and damping constant, respectively, of the *q*th-vibrational mode of the adsorbate and ω_{IR} is the frequency of the IR pulse. The nonresonant part, $\chi^{(2)}_{NR,eff}$, is the product of the susceptibility tensor elements of the Au substrate and Fresnel coefficients and can be considered to be constant for a given SFG spectrum in the form of a nonresonant amplitude $A_{NR,eff}$ and phase δ.

The SFG spectra of PDI, BPDI, and TPDI on gold are dominated by strong bands at 2183, 2188, and 2194 cm^{-1}, respectively, which are blue-shifted by ∼60 cm^{-1} when compared to the spectra of the free diisocyanides in KBr or as pure solids.[30,32,40,50] These strong bands are attributed to the NC group bound to the Au surface.[29,30,32] In addition, a weak peak around 2128 cm^{-1} can be observed for all samples, which has been assigned to the free NC groups not bound to the gold surface.[30,32,51−53] Moreover, the peak width of bound NC stretching mode (15−18 cm^{-1}) is much larger than the free NC mode (∼9 cm^{-1}), which can be attributed to the inhomogeneity of the adsorption sites on the polycrystalline gold surface.[29,32,41] These results are consistent with previous IR, SERS, and SFG studies showing that aromatic diisocyanides adsorb on gold surfaces through only one NC group while the other NC group points away from the surface.[29,30,32,40,42,51,53]

Electrochemical Stark Shift of Diisocyanide at Au/Liquid Interfaces. Figures 2a−c show representative potential-dependent SFG spectra of PDI, BPDI, and TPDI SAMs bound to Au electrodes, immersed in supporting electrolyte of a 0.1 M NaClO$_4$ aqueous solution. Potential-dependent SFG spectra for the three diisocyanide SAMs were measured using an *in situ* electrochemical SFG setup, described in the Supporting Information (Figure S1). The SAMs were found to be stable in the potential range between +0.1 and −0.7 V vs Ag/AgCl. Desorption of diisocyanide molecules from the gold surface occurs when the potential is more negative than −0.9 V or more positive than +0.1 V. As shown in Figures 2a−c, these spectra are dominated by the bound NC stretching mode, whose frequency shifts significantly with applied potential. In addition, weak free NC peaks can be also
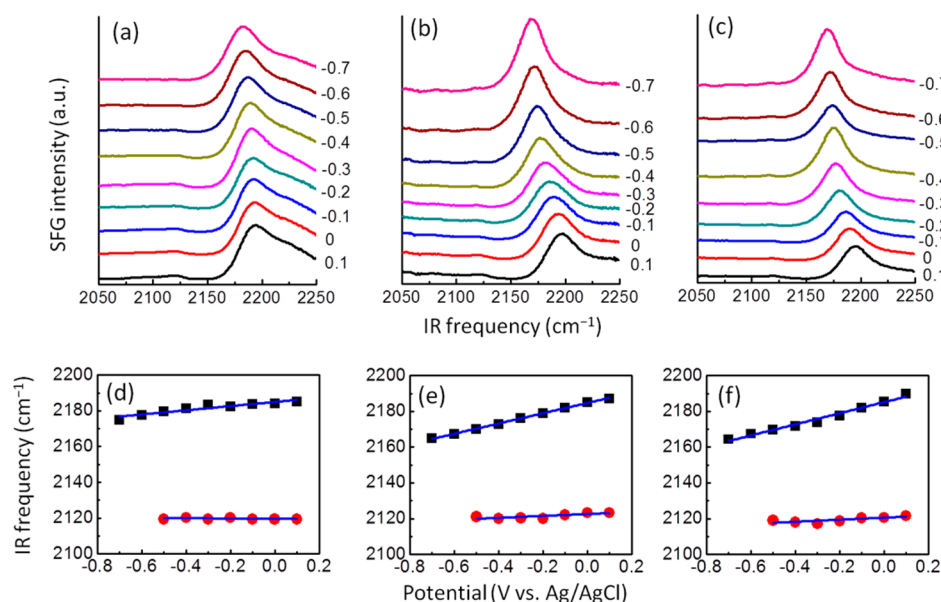
Figure 2. Bias-dependent SFG spectra. Representative potential-dependent SFG spectra of (a) PDI, (b) BPDI, and (c) TPDI SAMs on gold electrodes with 0.1 M NaClO$_4$ solution as electrolyte. The potentials (vs Ag/AgCl) are given in the panels. The spectra are offset for clarity. Lower panels present the corresponding potential-dependent frequencies of bound NC and free NC groups for (d) PDI, (e) BPDI, and (f) TPDI SAMs. Black squares represent measured frequencies of bound NC groups based on spectral fits. Red circles represent estimated frequencies of free NC groups. Blue lines are linear fits.

Table 1. Bias-Dependent Frequency and Field of Bound NC and Free NC Groups for PDI, BPDI, and TPDI SAMs on Au with 0.1 M NaClO$_4$ Aqueous Solution as the Electrolyte

SAM/Au		$d\omega/d\phi$ [cm^{-1}/V][b]		$\Delta\mu$ [cm^{-1}/(MV/cm)][c]		$dF/d\phi$ [10^8 (V/m)/m)][d]	
molecule	L [Å][a]	bound	free	bound	free	bound	x_2 [Å][e]
PDI	9.8	16 ± 4	1 ± 3	−1.8 ± 0.1	0.3 ± 0.1	9 ± 3	9.8 ± 3.4
BPDI	14.1	23 ± 3	2 ± 5	−1.6 ± 0.1	0.1 ± 0.1	15 ± 3	6.9 ± 1.5
TPDI	18.3	21 ± 6	7 ± 2	−1.5 ± 0.1	0.0 ± 0.1	14 ± 5	7.1 ± 2.6

[a]Estimated thickness of the SAM (DFT molecular length + C−Au bond). [b]Experimentally measured $d\omega/d\phi$ with error bars estimated from linear regression. [c]DFT-calculated Stark tuning rate ($\Delta\mu$) used in eq 2 with error bars estimated from linear regression. [d]Derivative of field vs applied potential ($dF/d\phi$) calculated using experimentally measured $d\omega/d\phi$ and computed $\Delta\mu$ according to eq 3 for bound NC. [e]Helmholtz layer thickness, determined from $dF/d\phi$ according to eq 5.

observed for SFG spectra measured between 0.1 and −0.4 V. At more negative potentials, the free NC stretching modes cannot be clearly resolved due to destructive interference with the much stronger signal of the bound NC stretching mode.

Figures 2d−f show the corresponding frequencies of the bound and free NC stretches as a function of applied potentials. The experimental frequencies of the bound NC are obtained from fits to the spectra, according to eq 1, with fitting results shown in Figure S2, and the fitting parameters listed in Table S4. The peak positions of the free NC are estimated from the raw SFG spectra directly because they cannot be precisely determined by fitting. These results show that the frequency of the NC stretch increases linearly with the applied potential. The slope of the increase, i.e., $d\omega/d\phi$, shows significant variation between SAM/Au samples prepared from the same molecules (see Table S5 for details) which is an indication of sample variation. In Table 1, we report the averaged $d\omega/d\phi$ values obtained from multiple samples, which are 16, 23, and 21 cm^{-1}/V for PDI, BPDI, and TPDI, respectively. The result of PDI on Au is similar to previous observations using SERS.[40,42] The frequency shifts of the free NC mode are significantly lower than those for the bound NC, with $d\omega/d\phi$ values near zero (Table 1).

The observed potential-dependent NC stretching frequency $\omega(\phi)$ can be related to the bias-dependent interfacial electric field $\overrightarrow{F}(\phi)$ through[9,16]

$$\omega(\phi) = \omega_0 - \overrightarrow{\Delta\mu} \cdot \overrightarrow{F}(\phi) \qquad (2)$$

in which ω_0 is the frequency in the absence of field and $\overrightarrow{\Delta\mu}$ is the difference in the dipole moment between the ground and excited vibrational states, also known as the Stark tuning rate. From eq 2, it is possible to relate the measured slope of frequency change as a function of bias $d\omega/d\phi$ to the derivative of the field with respect to the applied potential, according to eq 3.

$$\frac{dF}{d\phi} = -\frac{1}{\Delta\mu}\frac{d\omega}{d\phi} \qquad (3)$$

In eq 3, F and $\Delta\mu$ are the amplitudes of the field and Stark tunning rates, respectively, and we have assumed that the diisocyanide molecules stand perpendicular to the electrode surface (see below), with dipole change parallel with the interfacial field. Therefore, if $\Delta\mu$ can be independently determined by experiment or computational modeling, the SFG results can be used to determine *directly* the interfacial

field strengths and to test models of the interfacial structure, as shown in the following section based on DFT calculations of $\Delta\mu$.

DFT Calculation of SFG Spectra and Stark Tuning Rates. All DFT calculations were performed for Au_2 and Au_{10} model clusters with the Gaussian 09 Revision D.01 software package,[54] using the B3LYP hybrid functional,[55] the 6-311G++(d, p) basis set for nonmetals atoms, and the def2SVP pseudopotential and basis set for Au atoms.[56,57] Details of the methodology can be found in the Supporting Information (section 5). To validate the computational model, we first compare the experimental and DFT simulated SFG spectra of PDI, BPDI, and TPDI. As shown in Figure 1, the calculated spectra consist of a dominant intense signal at ~2185 cm^{-1} that corresponds to the Au−NC bound group and a weaker band at ~2130 cm^{-1} associated with the free NC (Table S6). These signals have opposite phases and interfere with each other and with the nonresonant background of Au, giving rise to the observed spectra. The overall agreement between simulated and experimental spectra is excellent, supporting the validity of gold cluster calculations to study the localized effect of the surface on the vibrational properties of the adsorbates and provide rigorous first principle interpretations of complex SFG spectra.[36,58,59]

A normal-mode analysis performed on these molecules reveals that upon binding to the surface each vibration becomes localized on each isocyanide bond (see Figure S3). Note that for an untethered molecule in the gas phase the two vibrations are mixed, giving rise to symmetric and asymmetric stretching modes. Binding to the surface breaks the degeneracy, localizing the vibrations on each CN and providing local modes that report on the field at a submolecular length scale. To characterize the nature of isocyanide bond to the Au surface, we carried out a detailed analysis of frontier orbitals in terms of projected density of states (see Figure S4 and Supporting Information for more details). The picture that emerges from the frontier orbital analysis shows that the diisocyanide/Au interaction is consistent with the well-known Blyholder model[60] with two competing interactions. On the one hand, donation of the carbon σ lone-pair electrons of the NC group to Au reduces the antibonding character of this orbital and, hence, increases the strength the NC bond. On the other hand, back-donation from the gold orbitals to the π^* orbitals of the NC group weakens the bond. For the present case, the former (σ donation) contribution is larger, and as a result, the NC frequency increases and the bond length decreases upon coordination to a gold surface (Table S6). Note that since the unbound NC group is only slightly affected by the surface, both its NC stretching frequency and bond length are similar to those found in the free molecule. These observations are consistent with previous studies[61,62] of diisocyanides bound to gold surfaces and support our DFT models.

To obtain $\Delta\mu$, we computed the change in ω_{NC} for both bound and free NC bonds after applying a uniform electric field along the Au−C bond in both positive and negative directions (see eq 2). For the bound group (Figure 3, top panel) the correlation of frequency and applied field (up to 10^9 V/m) is approximately linear. For the free NC case (Figure 3, bottom panel), the variation of frequency as a function of the applied field is less pronounced and displays some asymmetry between positive and negative fields. $\Delta\mu$ values determined from linear fits to the DFT data are shown in Table 1 (columns 5 and 6). Two issues are worth mentioning about the values reported in
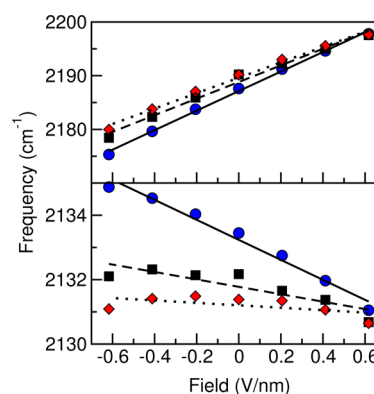

Figure 3. DFT field-dependent frequencies (symbols) of bound (top panel) and free (bottom panel) isocyanide groups along with the best linear fits (lines). PDI: blue circles, solid lines. BPDI: black squares, dashed lines. TPDI: red diamonds, dotted lines.

Table 1: (i) $\Delta\mu$ for bound and free NC have opposite signs, as expected from the different orientation of the two NC dipole moments; (ii) the magnitude of the Stark tuning rate for the bound NC is at least an order of magnitude larger than for the free NC, showing the dramatic effect of the surface on the susceptibility of the frequency shift, as shown by both the DFT dipole moment and molecular orbital descriptions (Supporting Information, section S6).

Electric Field Strength and Double-Layer Structure at Au/Liquid Interface. From the DFT Stark tuning rate, $\Delta\mu$, and the experimentally determined bias-dependent frequency change, $d\omega/d\phi$, we determine the change in field strength as a function of the applied bias, using eq 3. Table 1 lists the values of $dF/d\phi$ for the bound NC probes of PDI, BPDI, and TPDI. Determination of the absolute field strength at the electrode/electrolyte interface, as a function of the applied voltage, requires knowledge of the potential of zero charge, ϕ_{PZC}, of the gold−SAM system (i.e., the potential at which the net electric field is zero). The ϕ_{PZC} of evaporated Au electrode is ~0.2 V vs Ag/AgCl,[63] while the ϕ_{PZC} for the Au (111) single crystal surface and polycrystalline Au surfaces are ~0.3 V[64,65] and ~0 V,[66] respectively. Unfortunately, as the applied bias approaches +0.1 V, the diisocyanide SAM samples become unstable, preventing direct experimental measurement of ϕ_{PZC}. Assuming that ϕ_{PZC} is +0.2 V vs Ag/AgCl and using the values of $dF/d\phi$ reported in Table 1, the electric fields inside the SAMs are estimated to be in the range of $0.54 \times 10^8 - 1.1 \times 10^9$ V/m at applied potentials of +0.1 to −0.7 V, on the same order of magnitude as reported for the nitrile-terminated SAM on Au and Ag electrodes.[20]

The linear dependence of the probe frequency with the applied bias (Figure 2) suggests that the electric field at the NC group depends linearly on the applied bias (eq 3). To understand this dependence, we found it instructive to consider a simple electrostatic model based on the electric double-layer structure of a SAM-modified gold electrode shown in Figure 4.[20,67,68] In this model, we assume a Helmholtz layer between $x = 0$ and x_2 (in which there are no electrolytes) and a diffused layer of electrolytes at $x > x_2$. For the PDI SAM with high surface coverage, as used in this work, it has been shown that adsorbed PDI molecules orient perpendicularly to the surface.[52] Thus, for a fully ordered and well-packed SAM, x_2 corresponds to the length of SAM molecule plus the Au−C bond, which, as determined by DFT calculations, is 9.8, 14.1, and 18.3 Å for
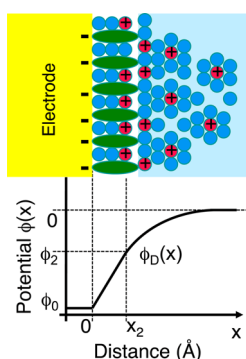
Figure 4. Top: model for Au/SAM/liquid interface. Bottom: schematic depiction of the variation of the potential across the electrode/liquid interface.

PDI, BPDI, and TPDI, respectively (Table 1). With electrolyte percolation into the SAM, x_2 can become smaller than the length of the molecule. The spatial distributions of the electrostatic potential and electric field strength at this electric double-layer model can be solved similarly to the Gouy−Chapman−Stern model.[1] Within this model, the field strength experienced by the probe molecule (and the bound isocyanide group) between $x = 0$ and x_2 is constant and is given by

$$F(0) = -\frac{\phi_2 - \phi_0}{x_2} \tag{4}$$

The field strength at x_2 can also be determined by the potential drop at the diffuse layer:

$$F(0) = \sqrt{\frac{8k_B T n^0}{\varepsilon \varepsilon_0}} \sinh\left(\frac{ze\phi_2}{2k_B T}\right) \tag{5}$$

In eqs 4 and 5 ϕ_0 and ϕ_2 are the potential, relative to the potential of zero charge (ϕ_{PZC}), at the electrode surface and x_2, respectively, ε (=78) is the dielectric constant of the aqueous solution, ε_0 is the permittivity, k_B is the Boltzmann constant, T is the absolute temperature in K, z (=1) is the absolute charge of the ion, e is the elementary charge, and n^0 is the electrolyte concentration. Using eqs 4 and 5, the derivative of the field with respect to the applied potential (ϕ_0) is given by eq 6, where k is the inverse Debye length.

$$\frac{dF(0)}{d\phi_0} = \frac{k \cosh\left(\frac{ze\phi_2}{2k_B T}\right)}{1 + kx_2 \cosh\left(\frac{ze\phi_2}{2k_B T}\right)} \tag{6}$$

According to eq 6, at large applied potentials, the field strength $F(0)$ becomes linearly dependent on the applied potential, with a slope of $1/x_2$. Thus, at this limit, the experimentally measured $d\omega/d\phi$ value can be used to determine the thickness of the Helmholtz layer via eqs 3 and 6. Although ϕ_{PZC} of Au can be affected slightly by SAM modification,[69,70] it is clear that most of the measurement range (0 to −0.7 V vs Ag/AgCl) falls in the large applied potential limit. As shown in Figures 2 and 3, the measured frequency varies linearly with the potential, consistent with this expectation. From the measured average $dF/d\phi$ values, we calculated the Helmholtz layer thicknesses x_2 to be 9.8 ± 3.4, 6.9 ± 1.5, and 7.1 ± 2.6 Å for PDI, BPDI, and TPDI, respectively (see Table 1). For PDI, the thickness is close to the length of the SAM, suggesting that the SAM is well packed with negligible amount of electrolyte inside the SAM.

For BPDI and TPDI, the Helmholtz layer thickness is shorter than the molecular length, suggesting that these SAMs are not as well packed and that there is significant penetration of the electrolyte inside the SAM. This is presumably the result of the relatively free rotation about the carbon−carbon bonds between phenyl rings of BPDI and TPDI and the rings sweeping out a larger volume between adjacent neighbors than would occur for strictly planar molecules. It is important to point out that there is considerable variation of the measured $d\omega/d\phi$ (and hence the x_2) values for different SAM covered electrodes prepared from the sample molecules (see Table S5). It likely reflects variation of the quality of the SAMs among these samples.

Molecular Dynamics of SAM on Gold. To gain microscopic insight into the structure of the electrode/liquid interface, we performed MD simulations of NaClO$_4$ aqueous solutions in contact with a PDI-coated (111) gold slab. The initial configuration for these simulations corresponds to two different PDI monolayer surface densities. On the basis of cyclic voltammetry measurements of PDI SAM in ferrocene/tetrabutylammonium hexafluorophosphate (TBAPF$_6$)/acetonitrile solution, we estimated that the gold surface coverage of PDI is roughly 20% (Supporting Information, section S7). Therefore, we attached PDI molecules to the gold surface on a regular grid using a (2 × 2) unit cell, which corresponds to a gold coverage of about 25%. For comparison, we also performed simulations using a ($\sqrt{3} \times \sqrt{3}$) unit cell of PDI arranged on the gold surface (coverage of about 33%). The model system was allowed to equilibrate with the aqueous electrolyte solution for 100 ps, and then a run of 2 ns was performed at constant temperature of 298 K to obtain statistical averages. Figure 5a shows a representative snapshot of the simulation cell (further details of the simulation procedure and parameters are provided in the Supporting Information, section S8).

Figure 5b shows the results for the water density distribution as well as the (center-of-mass) density distribution of ions, $\rho_i(z)$, as a function of distance from the gold slab for the ($\sqrt{3} \times \sqrt{3}$) SAM distribution. The density profiles were computed by dividing the simulation cell in 500 bins of width 0.2 Å and averaging the number of each species over 2 ns of the production run. The ion profiles reveal a very tightly adsorbed layer of anions at the monolayer surface (located at $z \approx 10$ Å, dashed vertical line) in contact with a more diffuse layer of cations that extend approximately 15 Å from the SAM interface into the bulk electrolyte. The alternation of negative and positive layers resembles the double-layer model and is similar to the oscillatory behavior found near graphene or metal electrodes in aqueous solutions[71,72] and molten salts.[73−75] The analysis of the water density distribution is also instructive. The presence of the monolayer produces some ordering of water molecules next to the SAM interface as evident from the peaks observed at $z = 9.6$ and 12.2 Å. Beyond 10 Å from the interface, the influence of the monolayer is negligible, and the bulk water density distribution is recovered. These results suggest that the well-packed ($\sqrt{3} \times \sqrt{3}$) monolayer does not allow for ion penetration, consistent with the values of the Helmholtz layer thickness found for PDI using the experimental measurements (Table 1).

Figure 5c shows the water and ion distributions for the 2 × 2 SAM model. The distributions of cations and anions are similar to those shown for the ($\sqrt{3} \times \sqrt{3}$) monolayer, with a slight shift (∼0.6 Å) of the maximum of the distribution of the anions
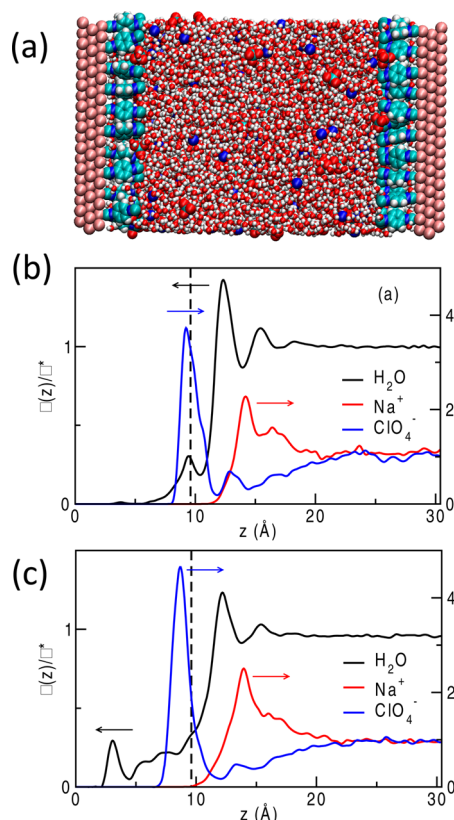
Figure 5. Molecular dynamics simulation of the electrochemical interface. (a) Typical molecular dynamics snapshot of 1 M NaClO$_4$ aqueous solutions in contact with a PDI-coated gold slab. (b, c) Density profiles for the water and ions (Na$^+$/ClO$_4^-$) as a function of distance to the gold slab for $\sqrt{3} \times \sqrt{3}$ (b) and 2×2 (c) model systems. Densities are normalized to the bulk value. In both graphs, the vertical dashed line indicates the thickness of the monolayer.

toward the interior of the monolayer. We note that water molecules can penetrate the PDI monolayer and get in close contact with the gold surface, as shown in the water density profiles inside the SAM region and the peak at $z = 3$ Å. Analysis of snapshots from the MD simulations reveals that within the SAM the solvent molecules are arranged in the form "water wires" that penetrate the monolayer from the bulk reservoir. Interestingly, this type of mechanism has been recently proposed to explain the ion permeability of nonpolar thiol-based monolayer in contact with electrolytes solutions at high voltage potentials.[76] Although a complete mechanistic analysis of this process for the case of isocyanide monolayer is beyond the scope of this study, the overall picture that emerges from these results suggest that although the ion distributions are quite insensitive to the SAM distribution, the permeability of the monolayer to water molecules is very sensitive to the arrangement of molecules on the electrode.

Figure 6 shows the mean electric potential across the monolayer for both $\sqrt{3} \times \sqrt{3}$ and 2×2 monolayer distributions. The electric potential was computed by numerical integration of the Poisson equation (eq 10):

$$\frac{d^2\Psi(z)}{dz^2} = -\frac{\rho_q(z)}{\varepsilon_0}$$

(10)

where $\rho_q(z)$ is the charge density (including the PDI charges) at a particular z position and ε_0 is the vacuum dielectric
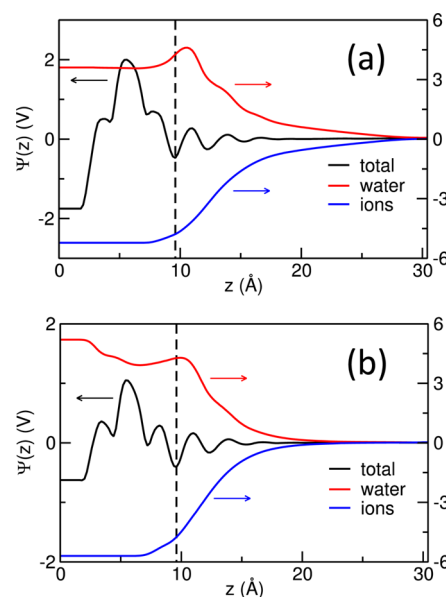

Figure 6. Mean electric potential profile as a function of the distance from the gold slab for $\sqrt{3} \times \sqrt{3}$ (a) and 2×2 (b) distributions. Also shown are the contribution of water and ions to the electric potential. Vertical dashed line indicates the thickness of the monolayer.

constant. Inside the monolayer and next to the interface, the electric potential exhibits significant oscillations due to the order distribution of water and ions and the order PDI monolayer.[71,73] After the oscillatory range, the electric potential reaches a constant value in the bulk region indicating screening of the potential. The decomposition of the potential profiles into contributions from water and from ions reveals that the permeability of the monolayer to the solvent slightly modulates the potential inside the SAM, as can be appreciated from the blue and red lines in Figure 6. It is interesting to note that the potential drop follows an exponential decay as expected from Debye−Hückel-like theories, 15 Å away from the gold, where the influence in the structure of electrolyte solution is negligible.

Although the oscillatory structure of the electric potential inside the monolayer is much more complex than modeled by mean-field or double-layer descriptions, it is still possible to estimate the electric field strength inside the SAM from Figure 6. Considering that the potential drop between the surface and the free NC is in the range 0.25−1.25 V and that the length of the monolayer is ∼10 Å, a mean-field approximation of the form $F = \Delta\Psi/\Delta z$ gives an electric field strength of the order of 10^8−10^9 V/m, which is in excellent agreement with the results obtained from the SFG experiment.

3. CONCLUSIONS

We employed *in situ* electrochemical vibrational SFG spectroscopy in combination with DFT calculations and MD simulations to study the electric double-layer structure at the aromatic diisocyanide SAM Au electrode/liquid interface. By comparing experimental and theoretical SFG spectra, we identify two NC stretching bands corresponding to bound and free NC groups, with the bound CN peaks at 2183, 2188, and 2194 cm^{-1} for PDI, BPDI, and TPDI, respectively, and the much weaker free NC peaks at ∼2128 cm^{-1}. The frequency of the bound NC stretching modes increases linearly with the applied potential (from −0.7 to +0.1 V versus Ag/AgCl, in 0.1

M NaClO$_4$ aqueous electrolyte), with slopes (dω/dϕ) of 16, 23, and 21 cm^{-1}/V for PDI, BPDI, and TPDI, respectively. A much smaller slope is observed for the free NC group. DFT calculations of model complexes reveal constant Stark tuning rate values within the experimental potential range. Our results suggest a linear dependence of interfacial field with applied bias with slopes (dF/dϕ) that can be computed from the observed dω/dϕ and computed Stark tuning rate. For an electrochemical double-layer model consisting of a Helmholtz layer and a diffused layer, the dF/dϕ value is a direct measure of the effective thickness of Helmholtz layer at large applied potentials. For PDI, the layer thickness is in good agreement of the molecular length, suggesting small to negligible penetration of electrolyte inside the SAM. For BPDI and TPDI, the effective layer thickness is much smaller than the molecular length, suggesting significant electrolyte penetration inside the SAM. Assuming a ϕ_{PZC} value of +0.2 V (vs Ag/AgCl) for aqueous 0.1 M NaClO$_4$ electrolyte, we found that the electric field is on the order of 10^8–10^9 V/m at the metal–electrolyte interfaces for all the isocyanide molecules studied in this work. Finally, PDI SAM/Au electrolyte interface was also modeled by molecular dynamics, revealing an electrochemical double-layer structure that is consistent with that deduced from the *in situ* electrochemical SFG measurement.

Our study demonstrates that electrochemical SFG spectroscopic measurement in combination with DFT calculation and molecular dynamics simulation can provide detailed molecular level understanding of electrochemical interfaces. We expect this integrated approach to be applicable to catalyst–metal and catalyst–semiconductor interfaces, providing a powerful tool for investigating the effects of interfacial field on the electro- and photocatalytic processes.

■ ASSOCIATED CONTENT

ⓢ Supporting Information

The Supporting Information is available free of charge on the ACS Publications website at DOI: 10.1021/acs.jpcc.7b05563.

> Sample preparation, experimental setup details, parameters of spectral fitting, measured Stark tuning rates for individual samples, DFT calculation and spectral simulation, Stark tuning rate calculated by DFT, estimation of surface coverage of PDI/Au SAM, details of molecular dynamics simulations, and additional references (PDF)

■ AUTHOR INFORMATION

Corresponding Authors

*(C.P.K.) E-mail ckubiak@ucsd.edu.
*(V.S.B.) E-mail victor.batista@yale.edu.
*(T.L.) E-mail tlian@emory.edu.

ORCID ⓞ

Benjamin Rudshteyn: 0000-0002-9511-6780
Clifford P. Kubiak: 0000-0003-2186-488X
Victor S. Batista: 0000-0002-3262-1237
Tianquan Lian: 0000-0002-8351-3690

Author Contributions

A.G. and P.E.V. made equal contributions.

Notes

The authors declare no competing financial interest.

■ REFERENCES

(1) Bard, A. J.; Faulkner, L. R.; Leddy, J.; Zoski, C. G. *Electrochemical Methods: Fundamentals and Applications*; Wiley: New York, 1980; Vol. 2.

(2) Schmickler, W.; Santos, E. *Interfacial Electrochemistry*; Springer Science & Business Media: 2010.

(3) Kamat, P. V. Manipulation of Charge Transfer across Semiconductor Interface. A Criterion That Cannot Be Ignored in Photocatalyst Design. *J. Phys. Chem. Lett.* **2012**, *3*, 663–672.

(4) Anderson, N. A.; Lian, T. Ultrafast Electron Transfer at the Molecule-Semiconductor Nanoparticle Interface. *Annu. Rev. Phys. Chem.* **2005**, *56*, 491–519.

(5) Ardo, S.; Sun, Y.; Staniszewski, A.; Castellano, F. N.; Meyer, G. J. Stark Effects after Excited-State Interfacial Electron Transfer at Sensitized TiO$_2$ Nanocrystallites. *J. Am. Chem. Soc.* **2010**, *132*, 6696–6709.

(6) Gorin, C. F.; Beh, E. S.; Kanan, M. W. An Electric Field–Induced Change in the Selectivity of a Metal Oxide–Catalyzed Epoxide Rearrangement. *J. Am. Chem. Soc.* **2012**, *134*, 186–189.

(7) Gorin, C. F.; Beh, E. S.; Bui, Q. M.; Dick, G. R.; Kanan, M. W. Interfacial Electric Field Effects on a Carbene Reaction Catalyzed by Rh Porphyrins. *J. Am. Chem. Soc.* **2013**, *135*, 11257–11265.

(8) Aragonès, A. C.; Haworth, N. L.; Darwish, N.; Ciampi, S.; Bloomfield, N. J.; Wallace, G. G.; Diez-Perez, I.; Coote, M. L. Electrostatic Catalysis of a Diels–Alder Reaction. *Nature* **2016**, *531*, 88–91.

(9) Chattopadhyay, A.; Boxer, S. G. Vibrational Stark Effect Spectroscopy. *J. Am. Chem. Soc.* **1995**, *117*, 1449–1450.

(10) Lambert, D. K. Vibrational Stark Effect of Adsorbates at Electrochemical Interfaces. *Electrochim. Acta* **1996**, *41*, 623–630.

(11) Weaver, M. J.; Wasileski, S. A. Influence of Double-Layer Solvation on Local Versus Macroscopic Surface Potentials on Ordered Platinum-Group Metals as Sensed by the Vibrational Stark Effect. *Langmuir* **2001**, *17*, 3039–3043.

(12) Wasileski, S. A.; Koper, M. T.; Weaver, M. J. Field-Dependent Electrode-Chemisorbate Bonding: Sensitivity of Vibrational Stark Effect and Binding Energetics to Nature of Surface Coordination. *J. Am. Chem. Soc.* **2002**, *124*, 2796–2805.

(13) Weaver, M. J. Electrostatic-Field Effects on Adsorbate Bonding and Structure at Metal Surfaces: Parallels between Electrochemical and Vacuum Systems. *Appl. Surf. Sci.* **1993**, *67*, 147–159.

(14) Lambert, D. K. Vibrational Stark Effect of CO on Ni (100), and CO in the Aqueous Double Layer: Experiment, Theory, and Models. *J. Chem. Phys.* **1988**, *89*, 3847–3860.

(15) Sorenson, S. A.; Patrow, J. G.; Dawlaty, J. M. Solvation Reaction Field at the Interface Measured by Vibrational Sum Frequency Generation Spectroscopy. *J. Am. Chem. Soc.* **2017**, *139*, 2369–2378.

(16) Suydam, I. T.; Boxer, S. G. Vibrational Stark Effects Calibrate the Sensitivity of Vibrational Probes for Electric Fields in Proteins. *Biochemistry* **2003**, *42*, 12050–12055.

(17) Suydam, I. T.; Snow, C. D.; Pande, V. S.; Boxer, S. G. Electric Fields at the Active Site of an Enzyme: Direct Comparison of Experiment with Theory. *Science* **2006**, *313*, 200–204.

(18) Fried, S. D.; Boxer, S. G. Measuring Electric Fields and Noncovalent Interactions Using the Vibrational Stark Effect. *Acc. Chem. Res.* **2015**, *48*, 998−1006.

(19) Fried, S. D.; Boxer, S. G. Electric Fields and Enzyme Catalysis. *Annu. Rev. Biochem.* **2017**, *86*, 387−415.

(20) Schkolnik, G.; Salewski, J.; Millo, D.; Zebger, I.; Franzen, S.; Hildebrandt, P. Vibrational Stark Effect of the Electric-Field Reporter 4-Mercaptobenzonitrile as a Tool for Investigating Electrostatics at Electrode/SAM/Solution Interfaces. *Int. J. Mol. Sci.* **2012**, *13*, 7466−7482.

(21) Oklejas, V.; Sjostrom, C.; Harris, J. M. SERS Detection of the Vibrational Stark Effect from Nitrile-Terminated Sams to Probe Electric Fields in the Diffuse Double-Layer. *J. Am. Chem. Soc.* **2002**, *124*, 2408−2409.

(22) Oklejas, V.; Sjostrom, C.; Harris, J. M. Surface-Enhanced Raman Scattering Based Vibrational Stark Effect as a Spatial Probe of Interfacial Electric Fields in the Diffuse Double Layer. *J. Phys. Chem. B* **2003**, *107*, 7788−7794.

(23) Baldelli, S. Probing Electric Fields at the Ionic Liquid-Electrode Interface Using Sum Frequency Generation Spectroscopy and Electrochemistry. *J. Phys. Chem. B* **2005**, *109*, 13049−13051.

(24) Angelici, R. J.; Lazar, M. Isocyanide Ligands Adsorbed on Metal Surfaces: Applications in Catalysis, Nanochemistry, and Molecular Electronics. *Inorg. Chem.* **2008**, *47*, 9155−9165.

(25) Seminario, J. M.; De La Cruz, C. E.; Derosa, P. A. A Theoretical Analysis of Metal-Molecule Contacts. *J. Am. Chem. Soc.* **2001**, *123*, 5616−5617.

(26) Heimel, G.; Romaner, L.; Zojer, E.; Brédas, J.-L. Toward Control of the Metal-Organic Interfacial Electronic Structure in Molecular Electronics: A First-Principles Study on Self-Assembled Monolayers of π-Conjugated Molecules on Noble Metals. *Nano Lett.* **2007**, *7*, 932−940.

(27) Petrovykh, D. Y.; Kimura-Suda, H.; Opdahl, A.; Richter, L. J.; Tarlov, M. J.; Whitman, L. J. Alkanethiols on Platinum: Multicomponent Self-Assembled Monolayers. *Langmuir* **2006**, *22*, 2578−2587.

(28) Kiguchi, M.; Miura, S.; Hara, K.; Sawamura, M.; Murakoshi, K. Conductance of Single 1, 4-Disubstituted Benzene Molecules Anchored to Pt Electrodes. *Appl. Phys. Lett.* **2007**, *91*, 053110.

(29) Robertson, M. J.; Angelici, R. J. Adsorption of Aryl and Alkyl Isocyanides on Powdered Gold. *Langmuir* **1994**, *10*, 1488−1492.

(30) Henderson, J. I.; Feng, S.; Bein, T.; Kubiak, C. P. Adsorption of Diisocyanides on Gold. *Langmuir* **2000**, *16*, 6183−6187.

(31) Rao, Y.; Turro, N. J.; Eisenthal, K. B. Solvation Dynamics at the Air/Water Interface with Time-Resolved Sum-Frequency Generation. *J. Phys. Chem. C* **2010**, *114*, 17703−17708.

(32) Swanson, S. A.; McClain, R.; Lovejoy, K. S.; Alamdari, N. B.; Hamilton, J. S.; Scott, J. C. Self-Assembled Diisocyanide Monolayer Films on Gold and Palladium. *Langmuir* **2005**, *21*, 5034−5039.

(33) Zhuang, X.; Miranda, P.; Kim, D.; Shen, Y. Mapping Molecular Orientation and Conformation at Interfaces by Surface Nonlinear Optics. *Phys. Rev. B: Condens. Matter Mater. Phys.* **1999**, *59*, 12632.

(34) Wang, H. F.; Gan, W.; Lu, R.; Rao, Y.; Wu, B. H. Quantitative Spectral and Orientational Analysis in Surface Sum Frequency Generation Vibrational Spectroscopy (SFG-VS). *Int. Rev. Phys. Chem.* **2005**, *24*, 191−256.

(35) Anfuso, C. L.; Snoeberger, R. C., III; Ricks, A. M.; Liu, W.; Xiao, D.; Batista, V. S.; Lian, T. Covalent Attachment of a Rhenium Bipyridyl CO_2 Reduction Catalyst to Rutile TiO_2. *J. Am. Chem. Soc.* **2011**, *133*, 6922−6925.

(36) Clark, M. L.; Rudshteyn, B.; Ge, A.; Chabolla, S. A.; Machan, C. W.; Psciuk, B. T.; Song, J.; Canzi, G.; Lian, T.; Batista, V. S.; et al. Orientation of Cyano-Substituted Bipyridine Re(I) *fac*-Tricarbonyl Electrocatalysts Bound to Conducting Au Surfaces. *J. Phys. Chem. C* **2016**, *120*, 1657−1665.

(37) Ge, A.; Rudshteyn, B.; Psciuk, B. T.; Xiao, D.; Song, J.; Anfuso, C. L.; Ricks, A. M.; Batista, V. S.; Lian, T. Surface-Induced Anisotropic Binding of a Rhenium CO_2-Reduction Catalyst on Rutile TiO_2 (110). *J. Phys. Chem. C* **2016**, *120*, 20970−20977.

(38) Yan, E. C. Y.; Fu, L.; Wang, Z.; Liu, W. Biological Macromolecules at Interfaces Probed by Chiral Vibrational Sum Frequency Generation Spectroscopy. *Chem. Rev.* **2014**, *114*, 8471−8498.

(39) Horswell, S. L.; O'Nei, I. A.; Schiffrin, D. J. Potential Modulated Infrared Reflectance Spectroscopy of Pt-Diisocyanide Nanostructured Electrodes. *J. Phys. Chem. B* **2001**, *105*, 941−947.

(40) Gruenbaum, S. M.; Henney, M. H.; Kumar, S.; Zou, S. Surface-Enhanced Raman Spectroscopic Study of 1, 4-Phenylene Diisocyanide Adsorbed on Gold and Platinum-Group Transition Metal Electrodes. *J. Phys. Chem. B* **2006**, *110*, 4782−4792.

(41) Kim, N. H.; Kim, K. Adsorption Characteristics of Arylisocyanide on Au and Pt Electrode Surfaces: Surface-Enhanced Raman Scattering Study. *J. Phys. Chem. B* **2006**, *110*, 1837−1842.

(42) Shin, D.; Kim, K.; Shin, K. S. Adsorbate-Induced Changes in Surface Potential of Gold Nanoparticles Revealed by Raman Spectroscopy. *ChemPhysChem* **2010**, *11*, 83−86.

(43) Baldelli, S. Surface Structure at the Ionic Liquid− Electrified Metal Interface. *Acc. Chem. Res.* **2008**, *41*, 421−431.

(44) Rey, N. G.; Dlott, D. D. Studies of Electrochemical Interfaces by Broadband Sum Frequency Generation. *J. Electroanal. Chem.* **2017**, DOI: 10.1016/j.jelechem.2016.12.023.

(45) Horowitz, Y.; Han, H.-L.; Ross, P. N.; Somorjai, G. A. In Situ Potentiodynamic Analysis of the Electrolyte/Silicon Electrodes Interface Reactions - A Sum Frequency Generation Vibrational Spectroscopy Study. *J. Am. Chem. Soc.* **2016**, *138*, 726−729.

(46) Braunschweig, B.; Mukherjee, P.; Dlott, D. D.; Wieckowski, A. Real-Time Investigations of Pt (111) Surface Transformations in Sulfuric Acid Solutions. *J. Am. Chem. Soc.* **2010**, *132*, 14036−14038.

(47) Yang, S.; Noguchi, H.; Uosaki, K. Electronic Structure of the CO/Pt(111) Electrode Interface Probed by Potential-Dependent IR/Visible Double Resonance Sum Frequency Generation Spectroscopy. *J. Phys. Chem. C* **2015**, *119*, 26056−26063.

(48) Gomes, J. F.; Busson, B.; Tadjeddine, A.; Tremiliosi-Filho, G. Ethanol Electro-Oxidation over Pt (*hkl*): Comparative Study on the Reaction Intermediates Probed by FTIR and SFG Spectroscopies. *Electrochim. Acta* **2008**, *53*, 6899−6905.

(49) Tong, Y.; Lapointe, F.; Thämer, M.; Wolf, M.; Campen, R. K. Hydrophobic Water Probed Experimentally at the Gold Electrode/Aqueous Interface. *Angew. Chem.* **2017**, *129*, 4275−4278.

(50) Han, H. S.; Han, S. W.; Joo, S. W.; Kim, K. Adsorption of 1, 4-Phenylene Diisocyanide on Silver Investigated by Infrared and Raman Spectroscopy. *Langmuir* **1999**, *15*, 6868−6874.

(51) Ito, M.; Noguchi, H.; Ikeda, K.; Uosaki, K. Substrate Dependent Structure of Adsorbed Aryl Isocyanides Studied by Sum Frequency Generation (SFG) Spectroscopy. *Phys. Chem. Chem. Phys.* **2010**, *12*, 3156−3163.

(52) Ghalgaoui, A.; Doudin, N.; Sterrer, M. Nanostructuring of Au (111) During Adsorption of an Aromatic Isocyanide from Solution. *Langmuir* **2017**, *33*, 91−99.

(53) Kim, H. S.; Lee, S. J.; Kim, N. H.; Yoon, J. K.; Park, H. K.; Kim, K. Adsorption Characteristics of 1,4-Phenylene Diisocyanide on Gold Nanoparticles: Infrared and Raman Spectroscopy Study. *Langmuir* **2003**, *19*, 6701−6710.

(54) Frisch, M. J.; Trucks, G. W.; Schlegel, H. B.; Scuseria, G. E.; Robb, M. A.; Cheeseman, J. R.; Scalmani, G.; Barone, V.; Mennucci, B.; Petersson, G. A.; et al. *Gaussian 09*, Revision D.01; Gaussian, Inc.: Wallingford, CT, 2009.

(55) Becke, A. D. Density-Functional Thermochemistry. III. The Role of Exact Exchange. *J. Chem. Phys.* **1993**, *98*, 5648−5652.

(56) Weigend, F.; Ahlrichs, R. Balanced Basis Sets of Split Valence, Triple Zeta Valence and Quadruple Zeta Valence Quality for H to Rn: Design and Assessment of Accuracy. *Phys. Chem. Chem. Phys.* **2005**, *7*, 3297−3305.

(57) Weigend, F. Accurate Coulomb-Fitting Basis Sets for H to Rn. *Phys. Chem. Chem. Phys.* **2006**, *8*, 1057−1065.

(58) Anfuso, C. L.; Xiao, D.; Ricks, A. M.; Negre, C. F. A.; Batista, V. S.; Lian, T. Orientation of a Series of CO_2 Reduction Catalysts on Single Crystal TiO_2 Probed by Phase-Sensitive Vibrational Sum

Frequency Generation Spectroscopy (PS-VSFG). *J. Phys. Chem. C* **2012**, *116*, 24107−24114.

(59) Chase, H. M.; Chen, S.; Fu, L.; Upshur, M. A.; Rudshteyn, B.; Thomson, R. J.; Wang, H.-F.; Batista, V. S.; Geiger, F. M. Orientations of Nonlocal Vibrational Modes from Combined Experimental and Theoretical Sum Frequency Spectroscopy. *Chem. Phys. Lett.* **2017**, *683*, 199−204.

(60) Blyholder, G. Molecular Orbital View of Chemisorbed Carbon Monoxide. *J. Phys. Chem.* **1964**, *68*, 2772−2777.

(61) Gilman, Y.; Allen, P. B.; Hybertsen, M. S. Density-Functional Study of Adsorption of Isocyanides on a Gold (111) Surface. *J. Phys. Chem. C* **2008**, *112*, 3314−3320.

(62) Li, Y.; Lu, D.; Swanson, S. A.; Scott, J. C.; Galli, G. Microscopic Characterization of the Interface between Aromatic Isocyanides and Au (111): A First-Principles Investigation. *J. Phys. Chem. C* **2008**, *112*, 6413−6421.

(63) Cai, W.-B.; Wan, L.-J.; Noda, H.; Hibino, Y.; Ataka, K.; Osawa, M. Orientational Phase Transition in a Pyridine Adlayer on Gold (111) in Aqueous Solution Studied by in Situ Infrared Spectroscopy and Scanning Tunneling Microscopy. *Langmuir* **1998**, *14*, 6992−6998.

(64) Kolb, D.; Schneider, J. Surface Reconstruction in Electrochemistry: Au (100-(5× 20), Au (111)-(1× 23) and Au (110)-(1× 2). *Electrochim. Acta* **1986**, *31*, 929−936.

(65) Stolberg, L.; Morin, S.; Lipkowski, J.; Irish, D. Adsorption of Pyridine at the Au (111)-Solution Interface. *J. Electroanal. Chem. Interfacial Electrochem.* **1991**, *307*, 241−262.

(66) Valette, G. Hydrophilicity of Metal Surfaces: Silver, Gold and Copper Electrodes. *J. Electroanal. Chem. Interfacial Electrochem.* **1982**, *139*, 285−301.

(67) Murgida, D. H.; Hildebrandt, P. Heterogeneous Electron Transfer of Cytochrome *c* on Coated Silver Electrodes. Electric Field Effects on Structure and Redox Potential. *J. Phys. Chem. B* **2001**, *105*, 1578−1586.

(68) Murgida, D. H.; Hildebrandt, P. Electron-Transfer Processes of Cytochrome *c* at Interfaces. New Insights by Surface-Enhanced Resonance Raman Spectroscopy. *Acc. Chem. Res.* **2004**, *37*, 854−861.

(69) Iwami, Y.; Hobara, D.; Yamamoto, M.; Kakiuchi, T. Determination of the Potential of Zero Charge of Au (111) Electrodes Modified with Thiol Self-Assembled Monolayers Using a Potential-Controlled Sessile Drop Method. *J. Electroanal. Chem.* **2004**, *564*, 77−83.

(70) Ramírez, P.; Andreu, R.; Cuesta, Á.; Calzado, C. J.; Calvente, J. J. Determination of the Potential of Zero Charge of Au (111) Modified with Thiol Monolayers. *Anal. Chem.* **2007**, *79*, 6473−6479.

(71) Willard, A. P.; Reed, S. K.; Madden, P. A.; Chandler, D. Water at an Electrochemical Interface—A Simulation Study. *Faraday Discuss.* **2009**, *141*, 423−441.

(72) Jiang, G.; Cheng, C.; Li, D.; Liu, J. Z. Molecular Dynamics Simulations of the Electric Double Layer Capacitance of Graphene Electrodes in Mono-Valent Aqueous Electrolytes. *Nano Res.* **2016**, *9*, 174−186.

(73) Pounds, M. A.; Salanne, M.; Madden, P. A. Molecular Aspects of the Eu^{3+}/Eu^{2+} Redox Reaction at the Interface between a Molten Salt and a Metallic Electrode. *Mol. Phys.* **2015**, *113*, 2451−2462.

(74) Merlet, C.; Rotenberg, B.; Madden, P. A.; Salanne, M. Computer Simulations of Ionic Liquids at Electrochemical Interfaces. *Phys. Chem. Chem. Phys.* **2013**, *15*, 15781−15792.

(75) Merlet, C.; Limmer, D. T.; Salanne, M.; van Roij, R.; Madden, P. A.; Chandler, D.; Rotenberg, B. The Electric Double Layer Has a Life of Its Own. *J. Phys. Chem. C* **2014**, *118*, 18291−18298.

(76) Kislenko, S.; Nikitina, V.; Nazmutdinov, R. A Molecular Dynamics Study of the Ionic and Molecular Permeability of Alkanethiol Monolayers on the Gold Electrode Surface. *High Energy Chem.* **2015**, *49*, 341−346.